

radarODE: An ODE-Embedded Deep Learning Model for Contactless ECG Reconstruction from Millimeter-Wave Radar

Yuanyuan Zhang, Runwei Guan, Lingxiao Li, Rui Yang, *Senior Member, IEEE*,
Yutao Yue, *Member, IEEE*, Eng Gee Lim, *Senior Member, IEEE*

Abstract—Radar-based contactless cardiac monitoring has become a popular research direction recently, but the fine-grained electrocardiogram (ECG) signal is still hard to reconstruct from millimeter-wave radar signal. The key obstacle is to decouple the cardiac activities in the electrical domain (i.e., ECG) from that in the mechanical domain (i.e., heartbeat), and most existing research only uses pure data-driven methods to map such domain transformation as a black box. Therefore, this work first proposes a signal model for domain transformation, and then a novel deep learning framework called radarODE is designed to fuse the temporal and morphological features extracted from radar signals and generate ECG. In addition, ordinary differential equations are embedded in radarODE as a decoder to provide morphological prior, helping the convergence of the model training and improving the robustness under body movements. After being validated on the dataset, the proposed radarODE achieves better performance compared with the benchmark in terms of missed detection rate, root mean square error, Pearson correlation coefficient with the improvement of 9%, 16% and 19%, respectively. The validation results imply that radarODE is capable of recovering ECG signals from radar signals with high fidelity and can be potentially implemented in real-life scenarios.

Index Terms—Contactless Cardiac Monitoring, Radio-Frequency Sensing, Deep Learning, Vital Sign Monitoring, Random Body Movement

I. INTRODUCTION

Radar-based human sensing is a rapidly evolving field that leverages radio-frequency signals to detect or recognize human

This work has been approved by University Ethics Committee, and is partially supported by Suzhou Science and Technology Programme (SYG202106), Jiangsu Industrial Technology Research Institute (JITRI) and Wuxi National Hi-Tech District (WND). (*Corresponding authors: Rui Yang, Yutao Yue.*)

Yuanyuan Zhang and Runwei Guan are with the School of Advanced Technology, Xi'an Jiaotong-Liverpool University, Suzhou, 215123, China, the Department of Electrical Engineering and Electronics, University of Liverpool, Liverpool, L69 3GJ, United Kingdom, and also with the Institute of Deep Perception Technology, JITRI, Wuxi, 214000, China (email: Yuanyuan.Zhang16@student.xjtu.edu.cn; Runwei.Guan21@student.xjtu.edu.cn).

Lingxiao Li is with the Multimedia Lab (MMLab), Department of Information Engineering, the Chinese University of Hong Kong, Shatin, N.T. 999077, Hong Kong (email: lingxiaoli@cuhk.edu.hk).

Rui Yang and Eng Gee Lim are with the School of Advanced Technology, Xi'an Jiaotong-Liverpool University, Suzhou, 215123, China (email: R.Yang@xjtu.edu.cn; Enggee.Lim@xjtu.edu.cn).

Yutao Yue is with the Thrust of Artificial Intelligence and Thrust of Intelligent Transportation, The Hong Kong University of Science and Technology (Guangzhou), Guangzhou 511400, China, and also with the Institute of Deep Perception Technology, JITRI, Wuxi 214000, China. (email: yutaoyue@hkust-gz.edu.cn).

activities in many future scenarios (e.g., smart home and in-cabin monitoring [1]–[3]). Compared with other contactless sensors such as cameras and acoustic sensors with privacy issues, radar could sense the ambient environment in a non-invasive manner and achieve good robustness under light conditions or temperature variations [4], [5]. In exchange, radar signals cannot be directly interpreted by humans like other mediums with explicit meanings (e.g., images, sound), increasing the complexity of designing efficient frameworks for specific sensing tasks (e.g., pose estimation [6], object detection [7] and vital sign monitoring [8]).

Within all scenarios suitable for radar-based human sensing, contactless vital sign monitoring is a crucial task in providing healthcare information (e.g., respiration, heart rate and electrocardiogram (ECG)). The earliest attempt for radar-based respiration monitoring can be traced back to 1975 by measuring the chest wall displacement induced by respiration [9]. The chest wall displacement will modulate the phase component of the emitted radar signal, and the latent respiration information can be demodulated from the phase variation [10]. Similarly, cardiac activities are small-scale displacements that also cause chest wall displacements, but such small displacements are normally ruined by respiration with orders more amplitude. The follow-up researchers are dedicated to extracting cardiac information in the presence of the respiration disturbance and also other common noises, such as random body movement (RBM) [11], [12], multi-path or multi-person interference [13], [14] and radar self-movement [15], [16].

In the context of cardiac monitoring, most early studies focused on the recovery of coarse cardiac information, such as heart rate (HR), heart sound and heart rate variability (HRV), from the perspectives of radar front-end design or advanced algorithms design [8]. For example, some advanced types of radar (e.g., frequency modulated continuous wave (FMCW) radar) are designed to enable high range-resolution or multi-person monitoring [17], and some baseband signal-processing algorithms are embedded on the radar platform to realize in-phase/quadrature modulation or accurate phase unwrapping [18]. In addition, various advanced algorithms are applied by leveraging different intrinsic characteristics of cardiac activities to robustly reconstruct cardiac features. For example, cardiac activities normally reveal strong periodicity in the time domain and have dominant peaks on the spectrum, inspiring periodicity-based methods (e.g., template matching [19], [20], hidden Markov model [21], [22]) and

spectrum-based methods (e.g., Fourier transform [23], [24], wavelet transform [7], [25]) as two major categories in cardiac feature extraction algorithms.

In recent years, the emergence of commercial radar platforms with high operating frequency (millimeter-wave (mm-wave) radar) encourages researchers to extract fine-grained cardiac features (e.g., ECG and seismocardiography (SCG)) from the radar signal [8]. SCG signal is measured by the accelerometer mounted on the human chest to describe the mechanical vibrations produced by heartbeats, describing the fine-grained cardiac mechanical activities such as aortic/mitral valve opening/closing and isovolumetric contraction [26]. Although these vibrations are subtle, it is still reasonable to directly map the displacements detected by radar to each fine-grained cardiac mechanical activity using high-resolution radar as proved in [17]. However, radar-based SCG recovery is not widely investigated compared with ECG, because ECG provides more comprehensive information (e.g., atrial/ventricular depolarization [27]) for clinical diagnosis.

To reconstruct ECG from radar signal, the most straightforward approach is to directly sense the scattered electromagnetic field variation through frequency shift of mm-wave response, and the ECG signal can then be decoupled from the scattered electromagnetic field based on the dynamic model in the form of partial differential equations deduced from cardiac electrophysiology (i.e., ionic concentration in cardiac cells) [28], [29]. However, the solutions of the entire model are extremely hard to obtain either numerically or analytically, and the constructed models will be changed with respect to different environments and noises due to the Green's function [30], causing difficulty in adapting the model in various real-life scenarios.

The second approach, which is also the most adopted approach, only uses radar to sense the cardiac mechanical activities through the phase-modulated mm-wave response as been investigated in coarse cardiac monitoring, but then the researchers must deal with domain decoupling to transform the measured signal from the mechanical domain to the electrical domain to generate the final ECG measurement. Intuitively, it is reasonable to say that mechanical conduction and electrical conduction are highly correlated in describing cardiac activities because the electrical changes in cells trigger the heart muscle contraction, whereas such a relationship is called excitation-contraction coupling in electrophysiology and is extremely hard to interpret or model by the people without biological knowledge [31], [32].

In literature, the existing studies all leverage deep learning methods to extract the latent information from enormous training data and try to learn the domain transformation relying on the extraordinary non-linear mapping ability of the deep neural network [33]–[36]. Although these studies could successfully reconstruct the ECG signal from radar, three drawbacks still need to be improved:

- There is no existing signal model with an easily understood form that can be integrated into domain transformation for radar-based ECG reconstruction.
- The pure data-driven method could learn the domain transformation as a black box, but the researchers can

hardly intervene in the learning process to enhance the characteristic peaks for ECG or provide prior knowledge to help with network training.

- The well-trained deep learning model is not robust to abrupt noises such as body movement [35], [37], because these noises normally have orders of magnitude larger than cardiac-related vibrations, drowning the subtle features and ruining the forward propagation of the deep neural network [38].

Inspired by the above discussions, this paper aims to design a framework for radar-based ECG reconstruction with ordinary differential equations (ODEs) embedded to provide prior knowledge on domain transformation. The contributions of this research can be concluded as:

- This study innovatively models the radar signal in terms of fine-grained cardiac features, enabling further transformation between cardiac mechanical and electrical activities, instead of using pure data-driven approaches as in the literature.
- Based on the proposed signal model, an ODE-embedded module called single cycle ECG generator (SCEG) is designed to parameterize the radar signal into sparse representations with morphological meanings, enhancing the characteristic peaks of the recovered ECG signal and also accelerating the convergence of the model training process.
- By fusing the extracted morphological and temporal features, the proposed radarODE framework is proven to be robust in the presence of body movement noise and could realize accurate reconstruction of the ECG signal from the millimeter wave radar signal.

The rest of the paper is organized as follows. Section II introduces the background knowledge required for radar-based ECG reconstruction. Section III explains the proposed model for radar signal and the structure of radarODE framework. Section IV first introduces the public dataset used for validation in this research and then presents the results obtained with corresponding comparisons and evaluations. Finally, Section V concludes this paper.

II. BACKGROUND

To understand the model and framework proposed later in this paper, this section will first provide the necessary background about the signal model for radar-based coarse cardiac monitoring and then briefly introduce the relationship between the cardiac electrical and mechanical activities.

A. Radar-Based Coarse Cardiac Monitoring

The vanilla signal model for radar-based cardiac monitoring (e.g., heart rate monitoring) using continuous wave (CW) radar starts from the transmitted signal expressed as

$$s_t(t) = A_t \cdot \cos(2\pi ft + \theta(t)) \quad (1)$$

where A_t and f are the amplitude and carrier frequency of the transmitted signal, and $\theta(t)$ is the phase noise from the signal generator with respect to time t [39]. In the ideal case, the

radar signal is only reflected by a human at a fixed distance d_0 with a varying chest displacement as $x(t)$, and the received signal after propagation time $T_p(t)$ can be derived as

$$s_r(t) = A_r \cdot \cos(2\pi f(t - T_p(t)) + \theta(t - T_p(t))) \quad (2)$$

with

$$\begin{aligned} T_p(t) &= \frac{2d(t)}{c} \\ d(t) &= d_0 + x(t) \end{aligned} \quad (3)$$

where A_r is the amplitude of the received signal, c is the light speed and $2d(t)$ represents the round trip distance of the signal between the transmitter and receiver. Then, the received signal can be expanded as

$$s_r(t) = A_r \cdot \cos\left(2\pi f t - \frac{4\pi d_0}{\lambda} - \frac{4\pi x(t)}{\lambda} + \theta\left(t - \frac{2d_0}{c} - \frac{2x(t)}{c}\right)\right) \quad (4)$$

where λ is the wavelength that equals to $\frac{c}{f}$. According to [39], [40], it is safe to eliminate the changes in amplitude and phase noise term because the chest displacement is much less than the fixed distance (i.e., $x(t) \ll d_0$). Therefore, the approximate received signal is

$$s_r(t) \approx \cos\left(2\pi f t - \frac{4\pi d_0}{\lambda} - \frac{4\pi x(t)}{\lambda} + \theta\left(t - \frac{2d_0}{c}\right)\right) \quad (5)$$

The received signal $s_r(t)$ will then pass a local oscillator with a low-pass filter to remove the frequency term, and the resultant baseband signal is

$$s_b(t) = \cos\left(\theta_d + \frac{4\pi x(t)}{\lambda} + \Delta\theta(t)\right) \quad (6)$$

with

$$\begin{aligned} \theta_d &= \frac{4\pi d_0}{\lambda} + \theta_0 \\ \Delta\theta(t) &= \theta(t) - \theta\left(t - \frac{2d_0}{c}\right) \end{aligned} \quad (7)$$

where θ_d , θ_0 and $\Delta\theta(t)$ are phase shifts affected by different factors such as d_0 , signal mixer and antenna, and can be set as constant in this paper [40]. Then, the phase signal unwrapped from the baseband signal is obtained as

$$\phi(t) = \theta_d + \frac{4\pi x(t)}{\lambda} + \Delta\theta(t) \quad (8)$$

Finally, the vanilla signal model derived above shows that the chest displacement $x(t)$ is involved in the phase variation of the baseband signal as

$$\Delta\phi(t) = \frac{4\pi x(t)}{\lambda} \quad (9)$$

The follow-up researchers have proposed various techniques to improve the accuracy of the unwrapped phase signal variation in (9). For example, the in-phase/quadrature modulation is proposed to solve the null point issue [39]; the differentiate and cross-multiply algorithm is designed to avoid discontinuity in the unwrapped phase signal [41]. In addition, chest displacement $x(t)$ is a mixture of cardiac activities, respiration and noises (e.g., RBM [11], [12], multi-path or multi-person interference [13], [14], [42]). Therefore, enormous advanced algorithms are proposed to decompose the cardiac information from $x(t)$, as have been reviewed in [8].

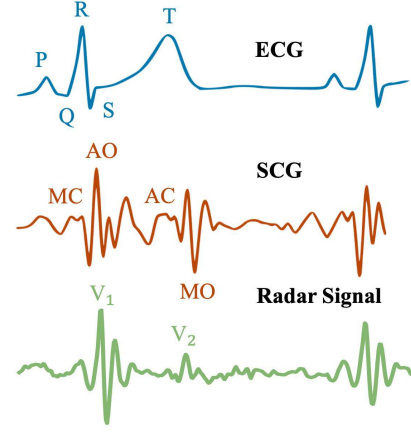


Fig. 1. Single cycle of ECG and SCG signals with corresponding cardiac activities and radar signal in the public dataset [35]

B. Radar-Based Fine-Grained Cardiac Monitoring

The coarse cardiac monitoring only aims to detect a single heartbeat within one cardiac cycle, and different cardiac features (e.g., HR, BBI and HRV) can then be calculated through the time indexes of a series of heartbeats. In contrast, fine-grained cardiac monitoring requires recovering as many cardiac activities as possible within one cardiac cycle. For example, Figure 1 shows the typical ECG and SCG signal waveform, representing the cardiac electrical and mechanical activities, respectively. ECG waveform comprises P-wave, QRS-complex and P-wave, corresponding to atrial depolarization, ventricular depolarization and ventricular repolarization, respectively. These electrical changes trigger the heart muscle contraction, causing the aortic valve opening/closure (AO/AC) and mitral valve opening/closure (MO/MC) [31], [32], as shown in the SCG plot in Figure 1. In addition, The relationship between cardiac electrical and mechanical activities is called excitation–contraction coupling in electrophysiology and can be modeled mathematically according to the intracellular calcium concentration, because calcium transient is the link between the action potential and muscle contraction [31], [32].

In the context of ECG reconstruction, two types of approaches in literature have been generalized in the Introduction section. The first approach is not considered in this paper because it involves complex modeling of electrophysiology from biology and chemistry [28]. This research only focuses on the second approach by reconstructing the ECG from the mechanical activities measured by radar. Although the underlying principle of the second approach is exactly the same as derived in (9), the radar signal should have a higher signal-to-noise ratio (SNR) and resolution than that used for coarse monitoring. For example, the mechanical activities can be simplified as the first vibration related to AO and the second vibration related to AC [17], corresponding to the QRS-complex and T-wave in the ECG signal. Therefore, the radar signal with high SNR and resolution should be able to reveal these two vibrations v_1 and v_2 as shown in the radar signal in Figure 1. In this case, only one public dataset [35] collected by 77 GHz FMCW radar satisfies the requirement

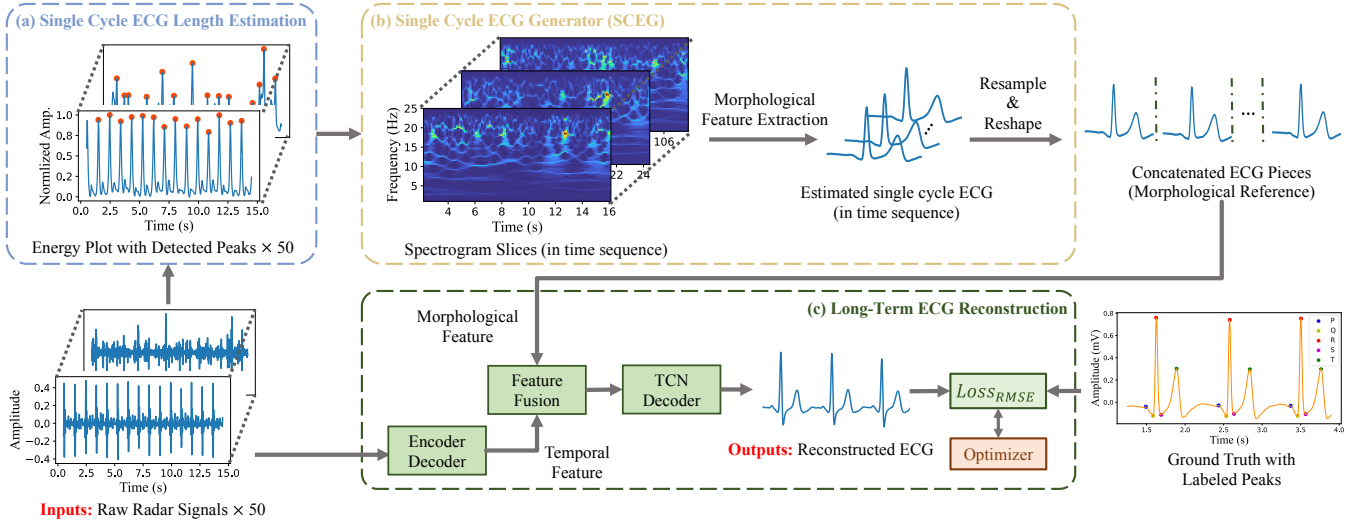


Fig. 2. Overview of the radarODE framework with three modules: (a) Single Cycle ECG Length Estimation; (b) Single Cycle ECG Generator; (c) Long-term ECG Reconstruction.

and complies with our proposed model in the next section.

III. METHODOLOGY

A. Overview

In order to address the drawbacks in radar-based ECG recovery as mentioned in the Introduction, this section will first introduce the proposed signal model that considers the nature of the fine-grained cardiac mechanical activities, ensuring a reasonable transformation towards cardiac electrical activities (ECG) instead of using pure data-driven methods as a black box. Afterwards, the proposed radarODE framework will be elaborated to fulfill the transformation from radar to ECG signal with 50 synchronous radar signals [35] as inputs, representing the measurements from 50 spatial points within the chest region as shown in Figure 2. The radarODE is composed of three modules to output the final ECG reconstructions as:

- The first module estimates the peak-to-peak interval (PPI) for consecutive heartbeats from the energy plot of the input radar signals based on the proposed peak detection algorithm, as shown in Figure 2(a).
- The second module first transforms the time-domain radar signal into spectrograms using synchrosqueezed wavelet transform (SST) to reveal the latent information in the frequency domain. Then, the morphological features (i.e., amplitudes and positions of PQRST peaks) for the single cycle ECG signal can be extracted from SST plots using the proposed SCEG, as shown in Figure 2(b).
- The third module is used to fuse the extracted morphological features with the temporal features hidden in the original radar signal to generate the final ECG recovery, as shown in Figure 2(c).

B. Model for Radar Signal and Pre-Processing

1) *Fine-Grained Model for Radar Signal*: According to the discussion in the last section, the chest displacement $x(t)$ can be further decomposed as

$$x(t) = x_c(t) + x_r(t) + x_n(t) \quad (10)$$

where $x_c(t)$ means cardiac mechanical activities, $x_r(t)$ is respiration induced displacement and $x_n(t)$ is noise term. After the pre-processing, the respiration term has been filtered out, and the actual radar signal $\tilde{x}(t)$ provided in the dataset [35] can be expressed as

$$\tilde{x}(t) = x_c(t) + x_n(t) \quad (11)$$

Furthermore, the pre-processed radar signal $\tilde{x}(t)$ has two prominent vibrations v_1 and v_2 as shown in Figure 1, corresponding to the fine-grained cardiac mechanical activities shown in SCG. According to the previous work on SCG modeling, the heart muscle contraction has a pulsatile nature [23], and the bones/tissues in chest area introduce the extra damping into the pulse [43]. Inspired by the natural characteristics, the radar signal with two prominent vibrations measured in a single cardiac cycle is innovatively modeled as the Gaussian pulses with certain central frequencies as

$$\tilde{x}(t) = v_1(t) + v_2(t) + x_n(t) \quad (12)$$

with

$$\begin{aligned} v_1 &= a_1 \cos(2\pi f_1 t) \exp\left(-\frac{(t - T_1)^2}{b_1^2}\right) \\ v_2 &= a_2 \cos(2\pi f_2 t) \exp\left(-\frac{(t - T_2)^2}{b_1^2}\right) \end{aligned} \quad (13)$$

where a_1, b_1 and a_2, b_2 jointly contribute to the amplitudes and length of the first and second prominent vibrations, f_1, f_2 are the corresponding central frequencies, T_1, T_2 determine when the vibrations happen, and $x_n(t)$ represents all the noises.

The aim of proposing the model in (12) is not to perform the curve fitting since the goal of this paper is ECG reconstruction but not SCG. In fact, the time indices of the vibrations (T_1 and T_2) are critical and need to be identified to help reconstruct QRS-complex and T-wave in ECG signals. In addition, to verify the fidelity of the proposed model in (12), a piece of high SNR radar signal $\tilde{x}(t)$ with the corresponding synthesis is shown in Figure 3. Empirically, the central frequencies of

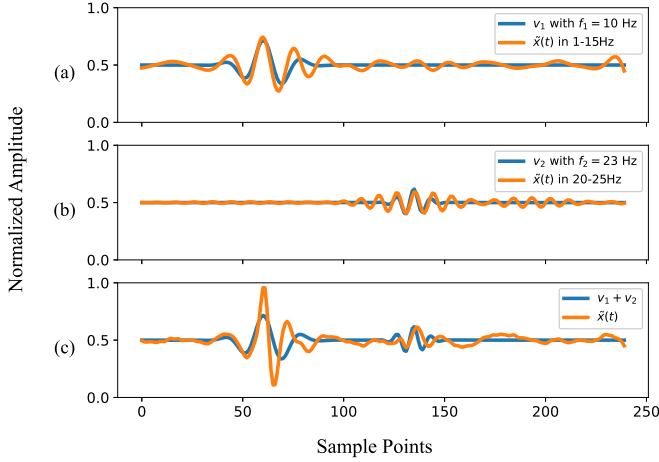


Fig. 3. True Radar signal with synthesis: (a) Synthesis for the first prominent vibration v_1 , with $a_1 = 0.22$, $b_1 = 0.05$, $f_1 = 10$ and $T_1 = -0.69$; (b) Synthesis for the second prominent vibration v_2 , with $a_2 = 0.12$, $b_2 = 0.03$, $f_2 = 23$ and $T_2 = -0.33$; (c) Overall synthesis with the ground truth radar signal.

v_1 and v_2 are laid in the range of $[1, 15]$ Hz and $[20, 25]$ Hz respectively, and all the unknown parameters can be obtained by solving the linear regression problem with respect to the band-passed radar signal. For example, Figure 3(a) shows the radar signal $\tilde{x}(t)$ filtered by the bandpass filter (BPF) with range $[1, 15]$ Hz, and the corresponding synthesis v_1 is obtained as $a_1 = 0.22$, $b_1 = 0.05$, $f_1 = 10$ and $T_1 = -0.69$. Similarly, the synthesis of the radar signal after BPF ($[20, 25]$ Hz) is shown in Figure 3(b) with $a_2 = 0.12$, $b_2 = 0.03$, $f_2 = 23$ and $T_2 = -0.33$. The overall result $v_1 + v_2$ shows that the synthesis based on the proposed model fits the original radar signal well, and the time indices of two vibrations can be found accurately.

Remark 1. Although the signal model proposed in this section is only used for the alignment between the cardiac mechanical and electrical features, this model actually describes the fundamental cardiac activities within a single cardiac cycle in a more realistic manner than only considering the single-tone heartbeat. Therefore, the proposed model is potentially universal to many other cardiac-related tasks as a template, such as heart rate monitoring, cardiac events segmentation and synthesis radar measurement generation/augmentation.

2) *Signal Pre-Processing with Synchrosqueezed Wavelet Transform (SST)*: Based on the proposed radar signal model in (12), the next step is to localize when the vibrations happen (i.e., T_1, T_2). Figure 1 shows that the high SNR radar signal could reveal prominent peaks of v_1 and v_2 in the time domain, but in most cases, these two peaks (especially v_2) could be ruined by the noise. Therefore, this research decides to extract the time-frequency domain information from the spectrogram obtained by synchrosqueezed wavelet transform (SST) [44], and the two vibrations can then be localized by the SCEG module proposed later in Section III-C2.

SST evolves from continuous wavelet transform (CWT) but with concentrated energy distribution along the frequency axis, providing a sparser time-frequency representation with

enhanced prominent vibrations compared with other tools such as short-time Fourier transform (STFT) and CWT.

The first step of SST is to calculate the CWT of radar signal $\tilde{x}(t)$ as

$$W_{\tilde{x}}(a, b) = \int \tilde{x}(t) a^{-1/2} \psi^* \left(\frac{t-b}{a} \right) dt \quad (14)$$

where ψ^* is the complex conjugate of the chosen mother wavelet, and a, b are the adjustable scaling and translation factors for the wavelet ψ to extract frequency- and time-domain information, respectively. In this research, the Morlet wavelet is selected as mother wavelet because it is widely used for vibration signal processing, especially for time-frequency localization [45], [46].

The second step is to calculate the candidate instantaneous frequency for $W_{\tilde{x}}(a, b) \neq 0$ as

$$f_{\tilde{x}}(a, b) = -2\pi i (W_{\tilde{x}}(a, b))^{-1} \frac{\partial W_{\tilde{x}}(a, b)}{\partial b} \quad (15)$$

The final step is to concentrate the energy along the candidate instantaneous frequency as

$$T_{\tilde{x}}(2\pi f, b) = \int_{A(b)} W_{\tilde{x}}(a, b) a^{-3/2} \delta(2\pi f_{\tilde{x}}(a, b) - 2\pi f) df \quad (16)$$

where $A(b) = \{a; W_s(a, b) \neq 0\}$, and δ represents the Dirac-delta function in a distribution version to smoothly squeeze the spread-out energy into a narrow band around the instantaneous frequency [44].

The resultant spectrograms obtained from the same piece of radar signal (Figure 4(a)) using different time-frequency representation tools are shown in Figure 4. The spectrogram yielded by STFT in Figure 4(b) could show the rough positions of each v_1 but cannot clearly reveal the position for v_2 . In comparison, CWT gives a sharp position for both vibrations, but the energy is still spread out and sometimes mixed with the background, as shown in Figure 4(c). By further concentrating the energy distribution, the spectrogram obtained by SST has a relatively clean background and sharp peaks for the vibrations as shown in Figure 4(d), reducing the burden of the deep-learning-based SCEG module in extracting latent features (i.e., T_1, T_2).

C. radarODE Framework Design

1) *Single Cycle ECG Length Estimation*: The first module of radarODE aims to estimate the length of each single cycle ECG piece by calculating the interval between two consecutive heartbeats (i.e., PPI), and these heartbeats will bring intensive energy into the received radar signal [21]. Therefore, the energy plots $\hat{x}(t)$ of the radar signal $\tilde{x}(t)$ can be obtained by simply adding the SST spectrogram along the frequency axis and are used for peak detection as shown in Figure 5a. In addition, it is found in practice that the algorithms designed for ECG R-peaks detection are also applicable for the peaks detection from the radar energy plot \hat{x} (omit (t) for simplicity) [47], because apparently the energy plot shares a similar upsurge with the ECG signal. However, the 50 synchronous radar signals provided in the dataset ($\{\tilde{x}_1, \dots, \tilde{x}_{50}\}$) do not

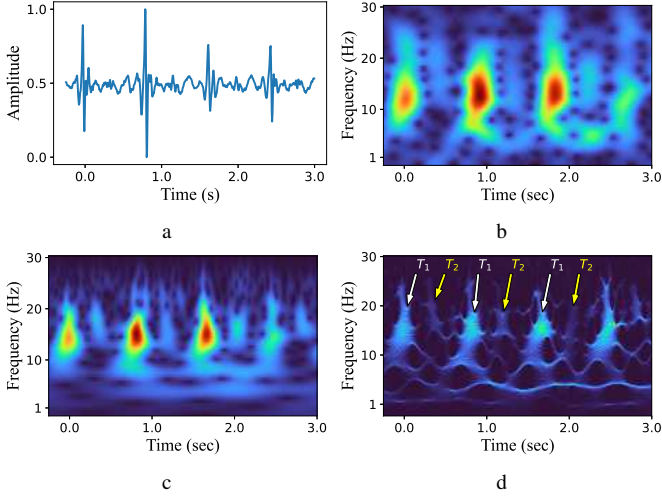


Fig. 4. Spectrograms obtained from the same radar signal: (a) Radar signal $\hat{x}(t)$; (b) STFT result; (c) CWT result; (d) SST result with T_1, T_2 labeled.

always have high SNR, potentially causing the wrong detection as shown in Figure 5b. Therefore, a new algorithm is proposed as in Algorithm 1 to eliminate the wrong detection obtained from 50 series of synchronous radar energy plots $X_{\mathcal{L}}$, with the length of each $\hat{x}_i \in X_{\mathcal{L}}$ equaling to l .

The design of Algorithm 1 is based on the fact that the PPI for healthy people tends to be unchanged in adjacent cardiac cycles. In this case, the long-term radar energy plots are firstly sliced into short segments as shown in the INITIALIZATION stage in Algorithm 1, and then the biopeaks algorithm [48] implemented in NeuroKit2 [47] is used for detecting all the potential peaks P from each energy plot segment \hat{x}_i^j as:

$$P = \text{biopeaks}(\hat{x}_i^j) \quad (17)$$

Secondly, the resultant PPI_C obtained from Line 8-10 in Algorithm 1 contains potential estimated PPI from 50 radar energy plots, with the correct estimations as the majority. Therefore, the kernel density estimation (KDE) [49] is applied on the candidate set PPI_C to calculate the probability density of different PPI values as:

$$\hat{f}(p) = \frac{1}{nh} \sum_{c=1}^n K\left(\frac{p - PPI_{c \in C}}{h}\right) \quad (18)$$

where $\hat{f}(p)$ means the estimated probability density function at point p , n is the number of all the estimated PPI in PPI_C , K represents the Gaussian kernel function and $h = n^{-1/5}$ is the bandwidth of the kernel. Lastly, the final PPI for the current segment is selected as argument p when $\hat{f}(p)$ achieves maximum as shown in Line 13 in Algorithm 1, and the long-term PPI estimation can be obtained step by step as the Algorithm 1 terminated.

Remark 2. Algorithm 1 actually provides an accurate PPI estimation for coarse cardiac monitoring tasks as demonstrated later in Section IV-C1, and can be directly used for the monitoring of heart rate and HRV.

2) *Single Cycle ECG Generator (SCEG)*: Based on the yielded PPI , the SST spectrogram can be sliced into segments

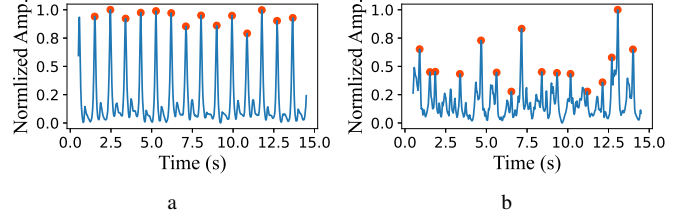


Fig. 5. Energy plot of the synchronous radar signals with different detected peaks: (a) Energy plot with high SNR and correct detection; (b) Energy plot with low SNR and wrong detection.

Algorithm 1 PPI Estimation

- 1: **Input:** Radar Energy Plots $X_{\mathcal{L}} = \{\hat{x}_1, \hat{x}_2, \dots, \hat{x}_{50}\}$, Segments Length l_{seg} and Step Length l_{step}
 - 2: **Output:** Estimated PPI
 - INITIALIZATION:
 - 3: - Let $X_S = \{X_{\mathcal{L}}^1, X_{\mathcal{L}}^2, \dots, X_{\mathcal{L}}^J\}$ be an ordered list of the segment lists sliced from $X_{\mathcal{L}}$ with length l_{seg} and step l_{step} , where $J = \frac{l - l_{seg}}{l_{step}}$.
 - 4: - Let $PPI \leftarrow \emptyset$.
 - MAIN ITERATION:
 - 5: **for** each segment list $X_{\mathcal{L}}^j \in X_S$ **do**
 - 6: - Let $PPI_C \leftarrow \emptyset$ to save the candidate PPI obtained from each segment.
 - 7: **for** each segment $\hat{x}_i^j \in X_{\mathcal{L}}^j$ **do**
 - 8: 1) Apply biopeaks [47] on \hat{x}_i^j to get all the detected peaks P as in (17).
 - 9: 2) Get PPI for the current radar signal segment using differentiation as $PPI_C \leftarrow \text{diff}(P)$.
 - 10: 3) Update $PPI_C \leftarrow PPI_C \cup PPI_C$.
 - 11: **end for**
 - 12: - Calculate the probability density function $\hat{f}(p)$ for PPI_C using KDE as in (18).
 - 13: - Determine the final PPI for the current segment list and update the set as $PPI \leftarrow PPI \cup \arg \max_p \hat{f}(p)$.
 - 14: **end for**
-

corresponding to a single cardiac cycle, and the aim of the SCEG module is to reconstruct the ECG for each single cardiac cycle, hence realizing the transformation from mechanical to electrical domain. In general, the input of the SCEG is N segments of the SST plot within $[1, 25]$ Hz with the size of $F \times T$ in frequency and time axis, and the output is the corresponding N pieces of ECG with the same length T , as shown in Figure 6. In practice, the deep neural network only accepts the inputs/outputs with the same size. Therefore, the actual SST segment is centered at the current cardiac cycle and expands to 4 seconds, and the corresponding ECG ground truth is resampled to a fixed length of 200 for loss calculation.

For the architecture design, the SCEG module adopts the popular backbone, encoder, and decoder structure as verified by enormous image-related tasks [50]–[52], with detailed parameters shown in Table I. In addition, a feature fusion block is added after the decoder to fuse the temporal and morphological features and generate the final ECG reconstruc-

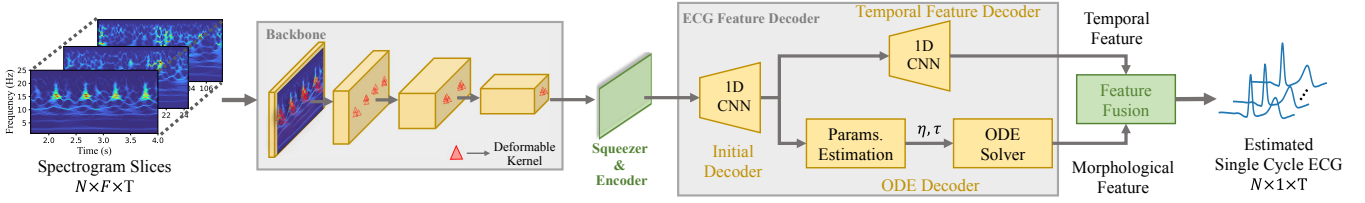


Fig. 6. Architecture of SCEG with SST segments as input and single cycle ECG pieces as output.

TABLE I
PARAMETERS USED FOR SCEG

Layers	Parameters (C_{in} , C_{out} , K , S) ¹	Output Shape N : Batch Size
Input SST		(N , 50, 71, 118)
a. Backbone		
Residual Block	(50, 128, (2, 1), (2, 1))	(N , 128, 72, 118)
Downsample Block	(128, 128, (3, 2), (2, 2))	(N , 128, 36, 60)
Residual Block	(128, 256, (2, 1), (1, 1))	(N , 256, 37, 60)
Downsample Block	(256, 256, (3, 2), (2, 2))	(N , 256, 19, 31)
Residual Block	(256, 512, (2, 1), (1, 1))	(N , 512, 20, 31)
Downsample Block	(512, 512, (3, 3), (2, 1))	(N , 512, 10, 31)
Residual Block	(512, 1024, (2, 1), (1, 1))	(N , 1024, 11, 31)
Downsample Block	(1024, 1024, (3, 3), (2, 1))	(N , 1024, 6, 31)
b. Squeezer&Encoder		
Conv2d	(1024, 1024, (6, 1), (1, 1))	(N , 1024, 31)
Transconv1d Block	(1024, 512, 5, 3)	(N , 512, 95)
Transconv1d Block	(512, 256, 5, 3)	(N , 256, 287)
Transconv1d Block	(512, 128, 5, 3)	(N , 128, 863)
c. ECG Feature Decoder		
Initial Decoder		
Conv1d Block	(128, 64, 7, 2)	(N , 64, 430)
Conv1d Block	(64, 32, 7, 2)	(N , 32, 213)
Conv1d Block	(32, 16, 7, 1)	(N , 16, 209)
Conv1d Block	(16, 8, 5, 1)	(N , 8, 207)
Temporal Feature Decoder		
Conv1d	(8, 4, 7, 1)	(N , 4, 203)
Conv1d	(4, 2, 5, 1)	(N , 2, 201)
Conv1d	(2, 1, 2, 1)	(N , 1, 200)
ODE Decoder		
Linear Block	(8 * 207, 512, -, -)	(N , 512)
Linear Block	(512, 128, -, -)	(N , 128)
Linear Block	(128, 32, -, -)	(N , 32)
Linear Block	(32, 16, -, -)	(N , 16)
ODE Solver	-	(N , 1, 200)
d. Feature Fusion		
Feature Multiply	-	(N , 1, 200)
Stack	-	(N , 1, 4, 200)
Conv2d Block	(1, 16, (5, 5), (1, 2))	(N , 16, 2, 98)
Conv2d Block	(16, 32, (3, 3), (1, 2))	(N , 32, 2, 48)
Conv2d Block	(32, 64, (3, 3), (2, 2))	(N , 64, 1, 23)
Transconv1d Block	(64, 32, 5, 2)	(N , 32, 52)
Transconv1d Block	(32, 16, 5, 2)	(N , 16, 106)
Transconv1d Block	(16, 8, 3, 2)	(N , 8, 10, 211)
Transconv1d	(8, 4, 6, 1)	(N , 4, 206)
Transconv1d	(4, 2, 5, 1)	(N , 2, 202)
Transconv1d	(2, 1, 3, 1)	(N , 1, 200)
Output single cycle ECG piece		(N , 1, 200)

1. C_{in} : Input channel, C_{out} : Output channel, K : Kernel size, S : Stride

tions. The detailed implementation of each part in Table I with explanations can be elaborated as:

a. **Backbone**: Backbone is typically used as the first block to extract both low-level (e.g., color, edge) and high-level features (e.g., presence of specific pattern) from the input images. In the context of this research, the backbone

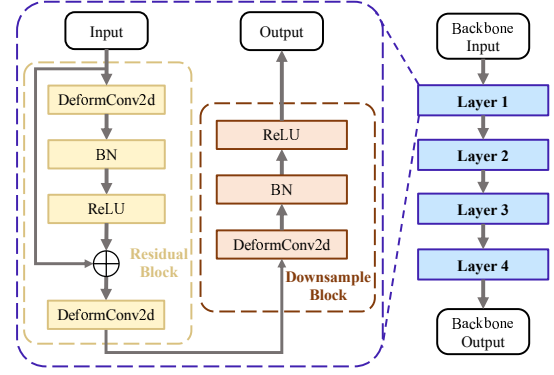


Fig. 7. Structure of backbone composed of residual block and downsample block: DeformConv2d means deformable 2D convolution, BN is batch normalization, and ReLU is the rectified linear unit activation function.

is expected to localize the vibrations v_1 , v_2 revealed as periodically appeared bright triangles within the range of $[1, 25]$ Hz on SST plots, providing latent information of T_1 , T_2 for the further ECG reconstruction.

According to the literature, the ResNet network with residual blocks is widely used as the backbone for feature extraction in many fields [53]–[55], and this research will use a similar structure with 4 layers of residual blocks and downsample blocks as shown in Figure 7, with the key parameters listed in Table I. In addition, the traditional 2D convolution is all replaced by deformable 2D convolution [56] with deformable kernels (instead of square kernels) to fit the irregular shape of the target patterns, as shown in red triangles in Figure 6.

- b. **Squeezer and Encoder**: The output feature map from the backbone should involve both frequency- and time-domain features, and the squeezer is simply used to squeeze the frequency-domain feature using 2D convolution (Conv2d) and output the feature map with the temporal feature only. Then, the encoder assembled by three 1D transposed convolution (Transconv1d) blocks is used to further extract the temporal feature, with each block comprising Transconv1d, BN and ReLU. Finally, the output feature map from the encoder should contain the latent information about the v_1 , v_2 (i.e., (T_1, T_2)).

- c. **ECG Feature Decoder**: The decoder is an essential part of SCEG to extract the temporal and morphological features separately from the latent information in the SST feature map, as shown in two branches in Figure 6. At first, an initial decoder is shared by the latter two decoders and comprises four 1D convolution (Conv1d) blocks with

Conv1d, BN, and ReLU inside. Similarly, the temporal feature decoder is assembled by three Conv1d, and the output feature should contain prominent peaks at the position of T_1, T_2 . However, these two peaks may still have deviations from the peaks in ECG ground truth, because obviously the mechanical vibrations v_1, v_2 lag behind QRS-complex and T-peaks, as shown in Figure 1. Another problem with the temporal feature decoder is that the ECG pieces have an entirely different shape with radar measurements, and the decoder needs to ‘memorize’ the unique pattern of ECG. Although the previous work shows the deep neural network could learn the patterns after training, the whole process of ECG reconstruction lacks supervision and is vulnerable to noise in radar signals [35], [57].

In this case, the ODE decoder is designed as a branch to assist the transformation between cardiac mechanical and electrical activities (radar to ECG) by introducing two prior facts in the real world:

- Although the biological one-to-one correspondence between cardiac electrical and mechanical activities (excitation–contraction coupling) is too complex to be modeled, it is safe to claim that the measurements of mechanical activities generally lag behind those of electrical activities with a short time delay τ [31], [32].
- The shape of the ECG piece can be modeled morphologically using ODEs without any biological/chemical knowledge [58], and the introduction of ODEs could provide morphological prior to accelerating the convergence of the model training process and also providing extra robustness in the presence of noises.

Inspired by the above two facts, the ODE decoder is designed as a parameters estimation part and an ODE solver as shown in Figure 6, and the solution of the ODEs will be shifted to the left with time τ . To be specific, the parameters estimation part contains four linear blocks (Linear Layer, BN, Tanh) to project the latent space yielded by the initial decoder into parameters η, τ , and η will be sent to an ODE solver to solve a 3D trajectory denoted by (x, y, z) as

$$\begin{cases} \frac{dx}{dt} = \alpha(x, y)x - \omega y \\ \frac{dy}{dt} = \alpha(x, y)y + \omega x \\ \frac{dz}{dt} = - \sum_{e_f \in \mathcal{F}} a_{e_f} \Delta \theta_{e_f}(x, y) e^{-\Delta \theta_{e_f}(x, y)^2 / 2b_{e_f}^2} - z \end{cases} \quad (19)$$

with

$$\begin{aligned} \alpha(x, y) &= 1 - \sqrt{x^2 + y^2} \\ \Delta \theta_{e_f}(x, y) &= (\theta(x, y) - \theta_{e_f}) \pmod{2\pi} \\ \theta(x, y) &= \text{atan} 2(y, x) \in [-\pi, \pi] \\ e_f \in \mathcal{F} &= \{e_P, e_Q, e_R, e_S, e_T\} \end{aligned} \quad (20)$$

where \mathcal{F} represents five characteristic peaks (PQRST) in a single cycle ECG signal, and the whole ODEs can be interpreted as manipulating each peak along a unit circle by varying the value of $\eta = \{a_{e_f}, b_{e_f}, \theta_{e_f}\}$ to adjust corresponding amplitude, width and position of each peak.

TABLE II
DEFAULT VALUES FOR η

$\eta \backslash \mathcal{F}$	eP	eQ	eR	eS	eT
a_{e_f}	5	-100	480	-120	8
b_{e_f}	0.25	0.1	0.1	0.1	0.4
θ_{e_f}	$-\frac{15\pi}{180}$	$\frac{25\pi}{180}$	$\frac{40\pi}{180}$	$\frac{60\pi}{180}$	$\frac{135\pi}{180}$

After specifying all 15 parameters η (3 for each peak) and the initial conditions of (x, y, z) , the value of z can be solved out by the ODE solver using Euler method to get the final single cycle ECG signal as the morphological feature. In practice, the default values for η are provided in advance as in Table II, and the estimated parameters within the range of $[-1, 1]$ are used to scale the default values.

- Feature Fusion:** The feature fusion module could leverage respective advantages of the morphological and temporal features and generate the final ECG signal for loss calculation, because the morphological feature only focuses on five peaks to provide a rough shape of ECG with calibrated peaks, and the temporal feature reserves all the other feature neglected in (19) to help the final reconstruction [59]. Therefore, two features are first fused together by multiplication into one and then stacked four times by itself. Then, the stacked feature is encoded and decoded as in Table I to yield the final single cycle ECG piece.

The last step of SCEG is to resample all the ECG pieces generated after the feature fusion part with respect to the previous PPI estimation, and the resampled ECG pieces are concatenated in time sequence to form the final morphological reference for long-term ECG reconstruction.

3) *Long-Term ECG Reconstruction:* The long-term ECG reconstruction network adopts a simpler encoder-decoder-fusion structure than SCEG as shown in Figure 2, because the morphological reference reduces the burden of learning the ECG peaks and patterns. In addition, the input changes to arbitrary segments of 50 synchronous time-domain radar signal instead of the SST segments within a single cardiac cycle. Therefore, the encoder for raw radar signal has the same structure as the backbone in SCEG, only with the deformable 2D convolution replaced by 1D convolution with $K = 5, S = 2$. Then, the decoder is performed by four Transconv1d blocks with the same K and S as an encoder to generate the temporal feature, and the feature fusion module also shares the same strategy as SCEG. Lastly, 9 stacks of the temporal convolutional network (TCN) with dilation fact of 2 are added as suggested in [35] to recursively generate the ECG based on the historical reconstructions.

IV. EXPERIMENTAL AND RESULT EVALUATION

A. Dataset and Benchmark Introduction

The dataset provided in [35] is collected by TI AWR-1843 radar with 77 GHz start frequency and 3.8 GHz bandwidth, providing good SNR and resolution to detect subtle vibrations that fit the proposed signal model and framework. Half of the actual dataset is released with 91 trials for 11 subjects,

and each trial contains 3 minutes of data (radar measurements and ECG ground truth) with 200 Hz sampling rate collected under 4 physiological statuses (i.e., normal breath (NB, 43 trials), irregular breath (IB, 18 trials), sleep (SP, 18 trials) and post exercise (PE, 12 trials)). In addition, the work in [35] has pre-processed the radar signal using several techniques, such as differentiator, dynamic time wrapping and clustering, to remove respiration noise preliminarily. Lastly, no existing study is found for ECG reconstruction in literature based on the same dataset, and the proposed framework MMECG in [35] will be used as the only benchmark to make a comparison with our radarODE.

In addition, the framework MMECG proposed in the same paper [35] is reproduced as the benchmark with 50 synchronous radar signal segments as input, because MMECG cannot handle SST spectrograms. In detail, MMECG utilizes Conv1d and Transformer [60] as the decoder to simultaneously extract temporal and spatial features, and the features are further fused by multiplication and then decoded by Transconv1d and TCN.

B. Implementation Details of radarODE

The proposed radarODE network is coded using PyTorch and trained for 200 epochs with batch size 32 on the NVIDIA RTX A4000 (16 GB) using stochastic gradient descent optimizer with early stop function [61] and learning rate 0.001 based on a cosine annealing schedule [62]. The dataset is split into training and testing sets based on 11-fold cross-validation for 11 subjects to ensure the mutually exclusive between training and testing. In addition, all the ground truth characteristic peaks, PPI, and cardiac cycles are obtained by the NeuroKit2 from ECG signals [48]. Furthermore, the 4-seconds-long input SST segments only contain the frequency component within [1, 25] Hz and are down-sampled to 30 Hz in the time-axis for saving memory usage. The input raw radar signal also needs to be segmented into 4-seconds-long pieces with a step of 0.2 seconds, and the output ECG pieces need to be further concatenated as 3 minutes long-term result as suggested in [35]. This research has been approved by University Ethics Committee of Xi'anJiaotong-Liverpool University with proposal number ER-SAT-0010000090020220906151929.

C. Experimental Results and Evaluations

1) *PPI Estimation*: The PPI estimation is the first module of radarODE, and the accuracy of the estimated PPI directly affects the fidelity of the concatenated morphological reference. Therefore, Figure 8a shows the PPI estimation error obtained by Algorithm 1 in terms of different subjects, using KDE or directly averaging the PPI from 50 radar signals. The large PPI error (e.g., for subject 13, 17) is normally caused by the body movements or residual respiration noise due to IB or PE statuses, as also shown in Figure 8b with large median error and variation for both methods. In contrast, the subjects in NB and SP statuses tend to be stable with less body movement, and the respiration noise can be well eliminated, achieving low median PPI error as 0.03 s and 0.02 s using the KDE-based method for each status. Overall, it is clear that the

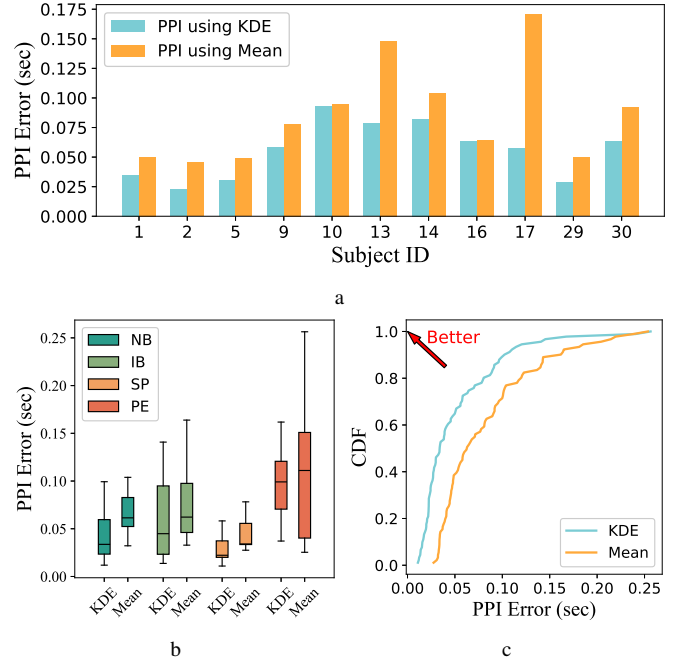


Fig. 8. PPI estimation error based on KDE and mean value: (a) View of different subjects; (b) View of different physiological statuses; (c) CDF for the overall PPI estimation error.

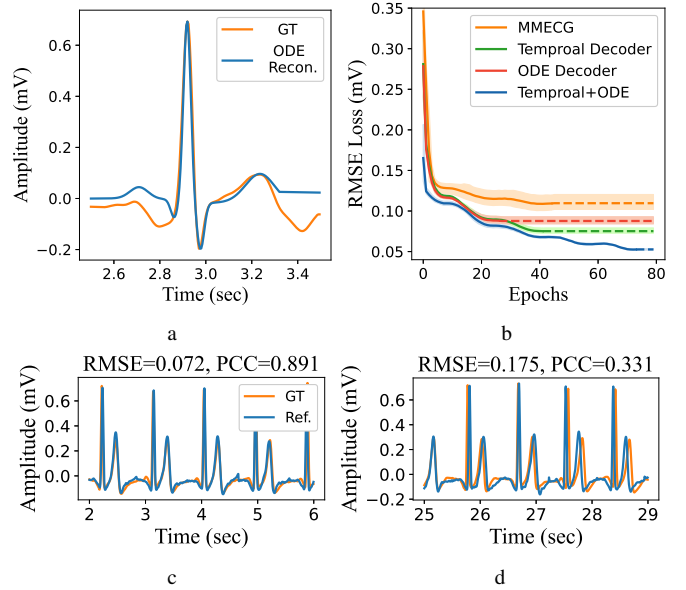


Fig. 9. Performance of SCEG: (a) Visualization of the rigid reconstruction (ODE Recon.) from ODE decoder with ground truth (GT) (b) Training loss comparison with benchmark and ablation study (without resampling); (c) and (d) High- and Low-fidelity of the generated morphological references (Ref.) with ground truth (GT), RMSE and correlation coefficient provided.

KDE-based PPI estimation is more accurate than the mean-based estimation for each subject, as shown in the cumulative distribution function (CDF) in Figure 8c, with the overall median PPI error of 0.03 s and 0.06 s respectively.

2) *Single Cycle ECG Generator (SCEG)*: The performance of the SCEG is only evaluated on the generated single cycle ECG pieces (without resampling and concatenation) in terms

TABLE III
COMPARISON WITH BENCHMARK AND ABLATION STUDY ABOUT TEMPORAL DECODER AND ODE DECODER (WITHOUT RESAMPLING)

Framework	Backbone	Encoder	Decoder	Fusion Method	RMSE (mV)	Correlation
MMECG [35]	-	Conv1d + Transformer	Transconv1d + TCN	Multiplication	0.091	87.9%
SCEG	DeformConv2d	Conv1d	Initial + Temporal	-	0.086	89.4%
			Initial + ODE	-	0.092	85.5%
			Initial + Temporal + ODE	Multiplication + Stack	0.077	92.6%

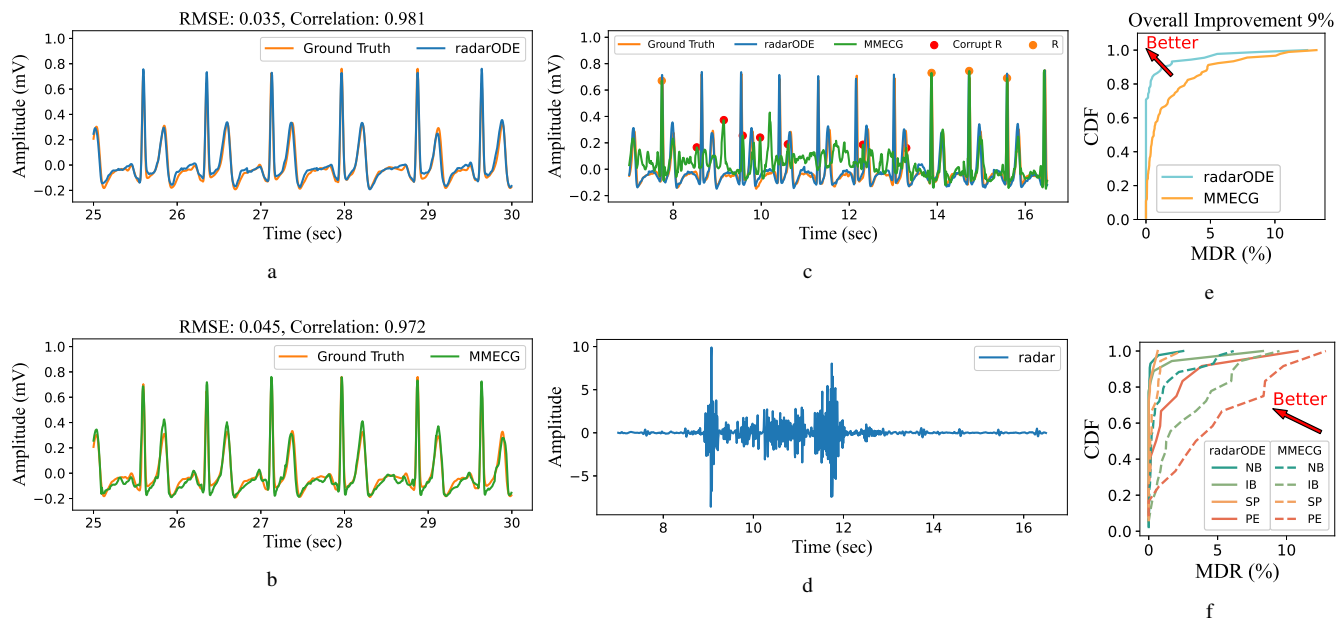


Fig. 10. Corrupt ECG reconstruction: (a) and (b) Ideal reconstruction results for radarODE and MMECG for the same period; (c) Corrupt ECG reconstruction yield by MMECG with corrupt R peaks detected, and faithful reconstruction from radarODE; (d) Raw radar signal during body movements, causing the previous corrupt reconstruction; (e) Overall missed detection rate (MDR); (f) MDR under different physical statuses for radarODE and MMECG.

of root mean square error (RMSE) and Pearson-correlation coefficient (PCC), because the aim of the SCEG module is only to generate ECG pieces while the PPI estimation error in resampling stage may affect the analysis of the actual performance of SCEG (e.g., a little deviation of the peak contributes to large RMSE). The detailed experimental results and evaluations are listed as:

a. Comparison with Benchmark and Ablation Study:

The overall performance for MMECG and radarODE in single cycle ECG generation are shown in Table III, with the median RMSE/PCC of 0.091 mV/87.9% and 0.077 mV/92.6%, respectively. In addition, to further evaluate the contributions of temporal and ODE decoders, the ablation study is implemented by only reserving one decoder without feature fusion. The results show that both decoders can work alone and achieve reasonable results as shown in Table III, but the ODE decoder has lower accuracy because it neglects the subtle ECG feature while only focusing on the characteristic peaks with rigid connections elsewhere, as shown in Figure 9a. However, the value of the ODE decoder will be revealed later in accelerating the training process and resisting body movements.

b. **Visualization of Training Process:** Figure 9b illustrates the training loss for benchmark and ablation study with the dotted line representing the early stop of the training

process and the shaded area indicating the repetition of the training process for five times. It is obvious that the ODE decoder itself cannot provide a very accurate reconstruction but could assist the entire model to achieve the lowest RMSE loss and also accelerate the convergence to achieve the RMSE of 0.17 mV after the first epoch.

c. **Performance after Resampling and Concatenation:** Although the SCEG could generate the ECG pieces with high fidelity, the resampled results will be affected by the PPI estimation error as shown in Figure 9c and 9d, because the slight deviation of the peak ruin the overall RMSE/PCC, hence requiring long-term reconstruction module to refine the concatenated ECG pieces in next step.

3) *Performance of radarODE:* The long-term ECG reconstruction module finally generates 3-minute-long ECG signals which will be used to evaluate the performance of the entire radarODE framework in terms of corrupt ECG reconstruction, morphological accuracy, and fine-grained cardiac feature accuracy as:

a. **Corrupt ECG Reconstruction:** The ideal reconstructed ECG signals are shown in Figure 10a and 10b with corresponding RMSE/PCC labeled. However, the long-term ECG signal may contain the corrupt parts due to the presence of the body movements (especially in IB and PE), because the scale of these body movements is

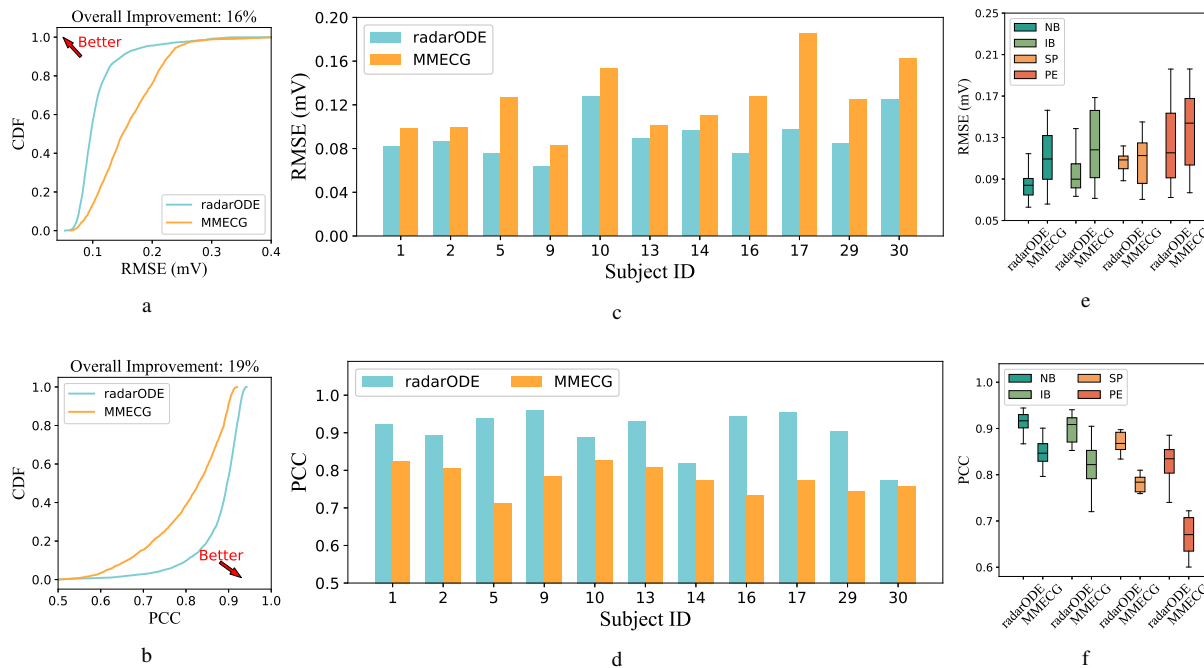


Fig. 11. Morphological Accuracy for radarODE and MMECG: (a) and (b) Overall CDF of RMSE and PCC for all trials; (c) and (d) RMSE and PCC under different physical statuses; (e) and (f) RMSE and PCC across all subjects.

much more extensive than the cardiac vibrations, hence drowning the subtle cardiac features. Figure 10c shows a piece of corrupted ECG reconstruction yield by MMECG with the falsely detected R peaks noted as red dots, and Figure 10d is the corresponding raw radar signal with extensive fluctuation induced by body movements. In contrast, the radarODE could still provide faithful ECG reconstructions under body movements due to the introduction of prior knowledge (ODE model) about ECG as the morphological reference, hence gaining certain robustness in resisting noises.

In the aims of quantifying the percentage of the corrupt reconstruction, three rules are made to reject the falsely detected R peaks yielded by Neurokit2 based on the empirical observations from all kinds of corrupt samples:

- The deviation of the corrupt R peak from the ground truth exceeds the absolute tolerance of 0.15 s [35].
- The corrupt R peak has one or several adjacent R peaks with the PPI smaller 0.3 s.
- The amplitude of the corrupt R peak is 30% lower than that of the ground truth R peak.

After filtering the corrupt R peaks from all detection, the overall missed detection rate (MDR) can be calculated by $MDR = \frac{\text{Remained R Peaks}}{\text{Ground Truth R Peaks}}$ as shown in Figure 10e, with the median MDR of 0% and 4.19%, and 90-percentile MDR as 1.34% and 4.76% for radarODE and MMECG respectively, and the overall improvement of radarODE compared with MMECG is 9%. In addition, the CDF plots for different physical statuses are plotted as in Figure 10f with the 90-percentile MDR of 0.12%, 0.85%, 0.32%, 3.71% during NB, IB, SP, PE for radarODE and 3.36%, 6.22%, 0.83%, 9.64% for MMECG. The result shows that different physical statuses have a noticeable impact on the

quality of the reconstructed long-term ECG, and radarODE could provide a higher MDR than MMECG in all statuses owing to the prior knowledge in the ODE decoder.

- b. **Morphological Accuracy:** The morphological accuracy can reveal the similarity between reconstructed and ground truth ECG signals by calculating RMSE and PCC, with RMSE mainly affected by the deviation of peaks and PCC focusing on the general shape. Figure 11a and 11b shows the overall performance of radarODE and MMECG in CDF with the median RMSE/PCC of 0.097mV/89.6% and 0.120mV/81.2%, and 90-percentile RMSE/PCC of 0.148mV/76.2% and 0.213mV/66.3%, respectively. The accuracy of the long-term ECG reconstruction is obviously lower than that of the single cycle ECG pieces in Table III, because the SCEG module only needs to learn the representations in one cardiac cycle with similar ECG patterns, but the long-term ECG reconstruction module deals with signals in arbitrary time period. Another critical remark is that the overall improvement of radarODE compared to MMECG is 16% and 19% for RMSE and PCC across 91 trials, indicating that the morphological prior is more helpful in generalizing the typical ECG pattern than calibrating the peaks.

In addition, Figure 11c and 11d shows the RMSE/PCC across all subjects, with radarODE always achieving better results than MMECG. In addition, the results of the long-term reconstruction show certain consistency with the previous PPI estimation error because the PPI error directly determines the fidelity of the morphological reference inputted in the long-term reconstruction module. For example, subjects 10, 13, 14, and 30 get worse results than others in either RMSE or PCC evaluation due to the large PPI estimation error as shown in Figure 8a.

Lastly, Figure 11e and 11f illustrate the RMSE/PCC for all trials in terms of different physical statuses, and radarODE outperforms MMECG across all the statuses. Additionally, the box plots for ECG recovery coincide with the PPI estimation error and show that the stable statuses (i.e., NB, SP) guarantee the reconstruction with small variance, while the unstable statuses (i.e., IB, PE) may heavily ruin the radar signal in some trials due to the body movements, causing an inconsistent quality of the reconstructed ECG. In addition, the trials for PE status are the least (only 12 trials) compared with the other three statuses, and the data shortage may also cause bad performance, because the training samples are not enough for deep neural networks to learn the pattern under PE status. However, radarODE could still provide the reconstructions with a smaller variance than MMECG, especially for unstable statuses because of the morphological prior embedded in the ODE decoder.

- c. **Fine-Grained Cardiac Events Reconstruction:** The evaluation of fine-grained cardiac features aims to analyze the temporal accuracy of the QRST peaks after filtering out the corrupt reconstructions. The P peak is not considered in this evaluation as also suggested in the benchmark paper [35], because the P peak is inconspicuous and even unable to be detected for some ground truth ECG pieces. The overall reconstructed ECG peak accuracy is shown in Figure 12a as CDF with the median/90-percentile absolute timing error for QRST peaks shown in Table IV. The results demonstrate that radarODE obtains a better peak accuracy than MMECG with the overall temporal error for QRST peaks improved by 5%, 23%, 37%, and 14%, respectively. The improvement is firstly attributed to the SST spectrogram with more evident patterns for reconstructing QRS-complex and T peak compared with using the time-domain signal as the input. Secondly, the ODE decoder itself cannot produce faithful reconstruction as shown in Figure 9a but could contribute to calibrating the peak positions according to η and τ , hence improving the overall peak accuracy. In addition, it is observed that the accuracy for the R peak is higher than the other peaks for both methods, because the deep neural network training relies on RMSE error and even a small deviation of the R peak with high amplitude causes large RMSE, hence the ‘learning’ of R peak becoming the most efficient way to reduce the RMSE loss.

TABLE IV
ABSOLUTE TIMING ERROR FOR RECONSTRUCTED ECG PEAKS

Framework	Percentile	Q	R	S	T
MMECG [35]	Median	0.021	0.012	0.019	0.018
	90-percentile	0.048	0.023	0.029	0.035
radarODE	Median	0.015	0.007	0.009	0.014
	90-percentile	0.027	0.015	0.020	0.023

unit: second

Figure 12b and 12c demonstrate the improvement of radarODE from the view of different physical statuses, and the results coincide with many previous evaluations. Firstly,

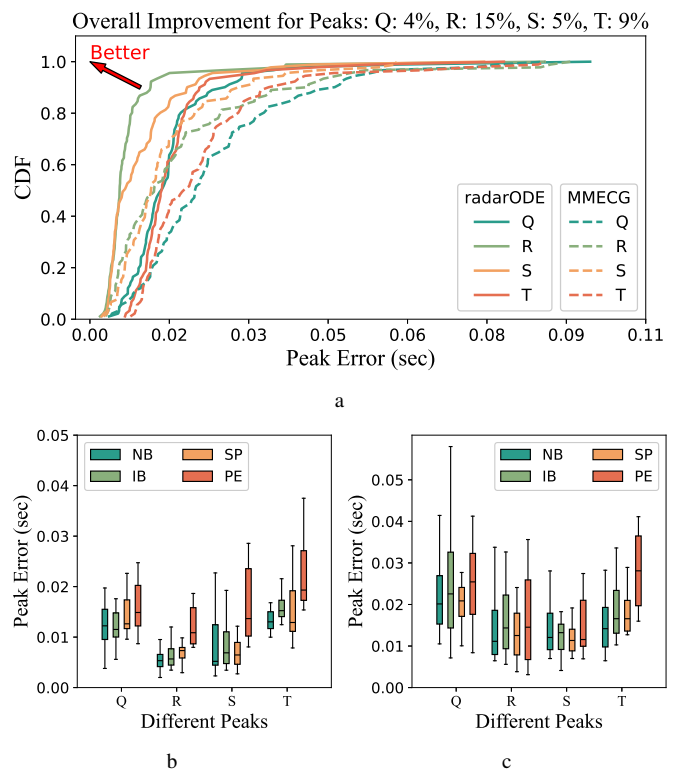


Fig. 12. Reconstructed ECG Peak Accuracy: (a) CDF of the overall temporal error for the reconstructed QRST peaks using radarODE and MMECG; (b) and (c) The peak error in terms of different physical statuses using radarODE and MMECG.

the radarODE performs better than MMECG for all statuses with R peak always achieving the best accuracy. Secondly, the stable physical statuses tend to yield accurate reconstruction with small variance, but the difference between statuses is smaller than that of the morphological accuracy analysis, because the corrupt reconstructions have been filtered for peak accuracy evaluation.

V. CONCLUSIONS

Radar-based ECG reconstruction is a critical technique in many future applications such as smart home and in-cabin monitoring, but the existing methods all apply the pure data-driven approaches, lacking the theoretical support regarding the transformation between mechanical activities measured by radar and electrical activities described as ECG. This research aims to bridge the gap to realize the transformation from the mechanical domain to the electrical domain by proposing the signal model with fine-grained features considered and further designing the deep learning framework radarODE with morphological prior embedding in the form of ODEs. The radarODE framework is validated on the public dataset containing 4.5 hours of radar measurements with corresponding ablation study, and the performance of the radarODE is also compared with the benchmark framework. The result evaluation shows that radarODE could achieve a better MDR, morphological accuracy and peak accuracy than the benchmark, proving the rationality of the proposed signal model and the effectiveness of the radarODE under various physical

statuses. In the future, the accuracy of the PPI estimation needs to be improved by using deep-learning-based methods, and several data augmentation techniques might be applied to alleviate the data shortages, especially for PE status.

REFERENCES

- [1] I. Nirmal, A. Khamis, M. Hassan, W. Hu, and X. Zhu, "Deep learning for radio-based human sensing: Recent advances and future directions," *IEEE Communications Surveys & Tutorials*, vol. 23, no. 2, pp. 995–1019, 2nd Quart. 2021.
- [2] J. Hu, H. Jiang, D. Liu, Z. Xiao, Q. Zhang, G. Min, and J. Liu, "Real-time contactless eye blink detection using uwb radar," *IEEE Transactions on Mobile Computing*, Oct. 2023.
- [3] F. Yao, Y. Ding, S. Hong, and S.-H. Yang, "A survey on evolved lora-based communication technologies for emerging internet of things applications," *International Journal of Network Dynamics and Intelligence*, pp. 4–19, Dec. 2022.
- [4] R. Guan, S. Yao, X. Zhu, K. L. Man, E. G. Lim, J. Smith, Y. Yue, and Y. Yue, "Achelus: A fast unified water-surface panoptic perception framework based on fusion of monocular camera and 4D mmWave radar," in *2023 IEEE 26th International Conference on Intelligent Transportation Systems (ITSC)*. IEEE, Sep. 2023, pp. 182–188.
- [5] F. Luo, S. Khan, A. Li, Y. Huang, and K. Wu, "Edgeactnet: Edge intelligence-enabled human activity recognition using radar point cloud," *IEEE Transactions on Mobile Computing*, Aug. 2023.
- [6] C. Yu, D. Zhang, Z. Wu, C. Xie, Z. Lu, Y. Hu, and Y. Chen, "MobiRFpose: Portable RF-based 3D human pose camera," *IEEE Transactions on Multimedia*, Sep. 2023.
- [7] M. Mercuri, I. R. Lorato, Y.-H. Liu, F. Wieringa, C. V. Hoof, and T. Torfs, "Vital-sign monitoring and spatial tracking of multiple people using a contactless radar-based sensor," *Nature Electronics*, vol. 2, no. 6, pp. 252–262, Jun. 2019.
- [8] Y. Zhang, R. Yang, Y. Yue, E. G. Lim, and Z. Wang, "An overview of algorithms for contactless cardiac feature extraction from radar signals: Advances and challenges," *IEEE Transactions on Instrumentation and Measurement*, Aug. 2023.
- [9] J. C. Lin, "Noninvasive microwave measurement of respiration," *Proceedings of the IEEE*, vol. 63, no. 10, pp. 1530–1530, Oct. 1975.
- [10] Y. Wang, W. Wang, M. Zhou, A. Ren, and Z. Tian, "Remote monitoring of human vital signs based on 77-GHz mm-wave FMCW radar," *Sensors*, vol. 20, no. 10, p. 2999, May 2020.
- [11] Z. Chen, T. Zheng, C. Cai, and J. Luo, "MoVi-Fi: Motion-robust vital signs waveform recovery via deep interpreted RF sensing," in *Proceedings of the 27th Annual International Conference on Mobile Computing and Networking (MobiCom)*, Feb. 2021, pp. 392–405.
- [12] J. Zhang, Y. Wu, Y. Chen, and T. Chen, "Health-radio: Towards contactless myocardial infarction detection using radio signals," *IEEE Transactions on Mobile Computing*, vol. 21, no. 2, pp. 585–597, Feb. 2022.
- [13] M. Mercuri, Y. Lu, S. Polito, F. Wieringa, Y.-H. Liu, A.-J. van der Veen, C. Van Hoof, and T. Torfs, "Enabling robust radar-based localization and vital signs monitoring in multipath propagation environments," *IEEE Transactions on Biomedical Engineering*, vol. 68, no. 11, pp. 3228–3240, Nov. 2021.
- [14] S. M. Islam, O. Boric-Lubecke, V. M. Lubecke, A.-K. Moadi, and A. E. Fathy, "Contactless radar-based sensors: Recent advances in vital-signs monitoring of multiple subjects," *IEEE Microwave Magazine*, vol. 23, no. 7, pp. 47–60, Jul. 2022.
- [15] S. D. Da Cruz, H.-P. Beise, U. Schröder, and U. Karahasanovic, "A theoretical investigation of the detection of vital signs in presence of car vibrations and radar-based passenger classification," *IEEE Transactions on Vehicular Technology*, vol. 68, no. 4, pp. 3374–3385, Apr. 2019.
- [16] S. Yang, D. Zhang, Y. Li, Y. Hu, Q. Sun, and Y. Chen, "iSense: Enabling radar sensing under mutual device interference," *IEEE Transactions on Mobile Computing*, Mar. 2024.
- [17] U. Ha, S. Assana, and F. Adib, "Contactless seismocardiography via deep learning radars," in *Proceedings of the 26th Annual International Conference on Mobile Computing and Networking (MobiCom)*, Apr. 2020, pp. 1–14.
- [18] A. B. Obadi, P. J. Soh, O. Aldayel, M. H. Al-Doori, M. Mercuri, and D. Schreurs, "A survey on vital signs detection using radar techniques and processing with FPGA implementation," *IEEE Circuits and Systems Magazine*, vol. 21, no. 1, pp. 41–74, Feb. 2021.
- [19] Q. Lv, L. Chen, K. An, J. Wang, H. Li, D. Ye, J. Huangfu, C. Li, and L. Ran, "Doppler vital signs detection in the presence of large-scale random body movements," *IEEE Transactions on Microwave Theory and Techniques*, vol. 66, no. 9, pp. 4261–4270, Sep. 2018.
- [20] T. Sakamoto, R. Imasaka, H. Taki, T. Sato, M. Yoshioka, K. Inoue, T. Fukuda, and H. Sakai, "Feature-based correlation and topological similarity for interbeat interval estimation using ultrawideband radar," *IEEE Transactions on Biomedical Engineering*, vol. 63, no. 4, pp. 747–757, Apr. 2015.
- [21] W. Xia, Y. Li, and S. Dong, "Radar-based high-accuracy cardiac activity sensing," *IEEE Transactions on Instrumentation and Measurement*, vol. 70, pp. 1–13, Jan. 2021.
- [22] Z. Mei, Q. Wu, Z. Hu, and J. Tao, "A fast non-contact vital signs detection method based on regional hidden Markov model in a 77GHz LFM CW radar system," in *IEEE International Conference on Acoustics, Speech and Signal Processing (ICASSP)*, May 2020, pp. 1145–1149.
- [23] M. Nosrati and N. Tavassolian, "Accurate Doppler radar-based cardiopulmonary sensing using chest-wall acceleration," *IEEE Journal of Electromagnetics, RF and Microwaves in Medicine and Biology*, vol. 3, no. 1, pp. 41–47, Mar. 2018.
- [24] J. Saluja, J. Casanova, and J. Lin, "A supervised machine learning algorithm for heart-rate detection using Doppler motion-sensing radar," *IEEE Journal of Electromagnetics, RF and Microwaves in Medicine and Biology*, vol. 4, no. 1, pp. 45–51, Mar. 2020.
- [25] M. Li and J. Lin, "Wavelet-transform-based data-length-variation technique for fast heart rate detection using 5.8-GHz CW Doppler radar," *IEEE Transactions on Microwave Theory and Techniques*, vol. 66, no. 1, pp. 568–576, Jan. 2017.
- [26] F. Cocconcelli, N. Mora, G. Matrella, and P. Ciampolini, "High-accuracy, unsupervised annotation of seismocardiogram traces for heart rate monitoring," *IEEE Transactions on Instrumentation and Measurement*, vol. 69, no. 9, pp. 6372–6380, Jan. 2020.
- [27] P. Khairy and A. J. Marelli, "Clinical use of electrocardiography in adults with congenital heart disease," *Circulation*, vol. 116, no. 23, pp. 2734–2746, Dec. 2007.
- [28] C. Xu, H. Li, Z. Li, H. Zhang, A. S. Rathore, X. Chen, K. Wang, M.-c. Huang, and W. Xu, "CardiacWave: A mmWave-based scheme of non-contact and high-definition heart activity computing," *Proceedings of the ACM on Interactive, Mobile, Wearable and Ubiquitous Technologies (IMWUT)*, vol. 5, no. 3, pp. 1–26, Sep. 2021.
- [29] A. Dong, A. Starr, and Y. Zhao, "Neural network-based parametric system identification: a review," *International Journal of Systems Science*, vol. 54, no. 13, pp. 2676–2688, Jul. 2023.
- [30] L. Li, Y. Shuang, Q. Ma, H. Li, H. Zhao, M. Wei, C. Liu, C. Hao, C.-W. Qiu, and T. J. Cui, "Intelligent metasurface imager and recognizer," *Light: Science & Applications*, vol. 8, no. 1, pp. 1–9, Oct. 2019.
- [31] L. M. Swift, M. W. Kay, C. M. Ripplinger, and N. G. Posnack, "Stop the beat to see the rhythm: excitation-contraction uncoupling in cardiac research," *American Journal of Physiology-Heart and Circulatory Physiology*, vol. 321, no. 6, pp. H1005–H1013, Dec. 2021.
- [32] R. Orkand and R. Niedergelke, "Heart action potential: dependence on external calcium and sodium ions," *Science*, vol. 146, no. 3648, pp. 1176–1177, Nov. 1964.
- [33] K. Yamamoto, R. Hiromatsu, and T. Ohtsuki, "ECG signal reconstruction via Doppler sensor by hybrid deep learning model with CNN and LSTM," *IEEE Access*, vol. 8, pp. 130 551–130 560, Jul. 2020.
- [34] W. Yin, X. Yang, L. Zhang, and E. Oki, "ECG monitoring system integrated with IR-UWB radar based on CNN," *IEEE Access*, vol. 4, pp. 6344–6351, Sep. 2016.
- [35] J. Chen, D. Zhang, Z. Wu, F. Zhou, Q. Sun, and Y. Chen, "Contactless electrocardiogram monitoring with millimeter wave radar," *IEEE Transactions on Mobile Computing*, Dec. 2022.
- [36] Y. Wu, H. Ni, C. Mao, and J. Han, "Contactless reconstruction of ECG and respiration signals with mmWave Radar based on RSSRnet," *IEEE Sensors Journal*, Nov. 2023.
- [37] Y. Wang, Z. Wang, J. A. Zhang, H. Zhang, and M. Xu, "Vital sign monitoring in dynamic environment via mmWave radar and camera fusion," *IEEE Transactions on Mobile Computing*, Jun. 2023.
- [38] P. Wang, X. Ma, R. Zheng, L. Chen, X. Zhang, D. Zeghlache, and D. Zhang, "SlpRoF: Improving the temporal coverage and robustness of RF-based vital sign monitoring during sleep," *IEEE Transactions on Mobile Computing*, Dec. 2023.
- [39] A. D. Droitcour, O. Boric-Lubecke, V. M. Lubecke, J. Lin, and G. T. Kovacs, "Range correlation and I/Q performance benefits in single-chip silicon Doppler radars for noncontact cardiopulmonary monitoring,"

- IEEE Transactions on Microwave Theory and Techniques*, vol. 52, no. 3, pp. 838–848, Mar. 2004.
- [40] H. Zhao, H. Hong, L. Sun, Y. Li, C. Li, and X. Zhu, “Noncontact physiological dynamics detection using low-power digital-IF Doppler radar,” *IEEE Transactions on Instrumentation and Measurement*, vol. 66, no. 7, pp. 1780–1788, Jul. 2017.
- [41] J. Wang, X. Wang, L. Chen, J. Huangfu, C. Li, and L. Ran, “Noncontact distance and amplitude-independent vibration measurement based on an extended DACM algorithm,” *IEEE Transactions on Instrumentation and Measurement*, vol. 63, no. 1, pp. 145–153, Aug. 2013.
- [42] C. Gao, X. He, H. Dong, H. Liu, and G. Lyu, “A survey on fault-tolerant consensus control of multi-agent systems: trends, methodologies and prospects,” *International Journal of Systems Science*, vol. 53, no. 13, pp. 2800–2813, Mar. 2022.
- [43] D. R. Morgan and M. G. Zierdt, “Novel signal processing techniques for Doppler radar cardiopulmonary sensing,” *Signal Processing*, vol. 89, no. 1, pp. 45–66, Jan. 2009.
- [44] I. Daubechies, J. Lu, and H.-T. Wu, “Synchrosqueezed wavelet transforms: An empirical mode decomposition-like tool,” *Applied and Computational Harmonic Analysis*, vol. 30, no. 2, pp. 243–261, Aug. 2011.
- [45] Y. Xue, R. Yang, X. Chen, Z. Tian, and Z. Wang, “A novel local binary temporal convolutional neural network for bearing fault diagnosis,” *IEEE Transactions on Instrumentation and Measurement*, Jul. 2023.
- [46] K. Griffiths, B. J. Hicks, P. Keogh, and D. Shires, “Wavelet analysis to decompose a vibration simulation signal to improve pre-distribution testing of packaging,” *Mechanical Systems and Signal Processing*, vol. 76, pp. 780–795, Aug. 2016.
- [47] J. C. Brammer, “Biopeaks: A graphical user interface for feature extraction from heart-and breathing biosignals,” *Journal of Open Source Software*, vol. 5, no. 54, p. 2621, Oct. 2020.
- [48] D. Makowski, T. Pham, Z. J. Lau, J. C. Brammer, F. Lespinasse, H. Pham, C. Schölzel, and S. A. Chen, “NeuroKit2: A Python toolbox for neurophysiological signal processing,” *Behavior Research Methods*, pp. 1–8, Feb. 2021.
- [49] G. R. Terrell and D. W. Scott, “Variable kernel density estimation,” *The Annals of Statistics*, pp. 1236–1265, Sep. 1992.
- [50] W. Zhang, B. Basaran, Q. Meng, M. Baugh, J. Stelter, P. Lung, U. Patel, W. Bai, D. Karampinos, and B. Kainz, “Mocosr: Respiratory motion correction and super-resolution for 3d abdominal mri,” in *International Conference on Medical Image Computing and Computer-Assisted Intervention*. Springer, Oct. 2023, pp. 121–131.
- [51] L. Li, Y. Zhang, and S. Wang, “The Euclidean space is evil: hyperbolic attribute editing for few-shot image generation,” in *Proceedings of the IEEE/CVF International Conference on Computer Vision*, Oct. 2023, pp. 22 714–22 724.
- [52] Z. Chu, R. Yan, and S. Wang, “Vessel turnaround time prediction: A machine learning approach,” *Ocean & Coastal Management*, vol. 249, p. 107021, Mar. 2024.
- [53] X. Chen, R. Yang, Y. Xue, B. Song, and Z. Wang, “TFPred: Learning discriminative representations from unlabeled data for few-label rotating machinery fault diagnosis,” *Control Engineering Practice*, vol. 146, p. 105900, Feb. 2024.
- [54] F. He, T. Liu, and D. Tao, “Why Resnet works? residuals generalize,” *IEEE Transactions on Neural Networks and Learning Systems*, vol. 31, no. 12, pp. 5349–5362, Feb. 2020.
- [55] C.-M. Liang, Y.-W. Li, Y.-H. Liu, P.-F. Wen, and H. Yang, “Segmentation and weight prediction of grape ear based on SFNet-ResNet18,” *Systems Science & Control Engineering*, vol. 10, no. 1, pp. 722–732, Aug. 2022.
- [56] J. Dai, H. Qi, Y. Xiong, Y. Li, G. Zhang, H. Hu, and Y. Wei, “Deformable convolutional networks,” in *Proceedings of the IEEE International Conference on Computer Vision*, 2017, pp. 764–773.
- [57] D. Yang, J. Lu, H. Dong, and Z. Hu, “Pipeline signal feature extraction method based on multi-feature entropy fusion and local linear embedding,” *Systems Science & Control Engineering*, vol. 10, no. 1, pp. 407–416, Apr. 2022.
- [58] P. E. McSharry, G. D. Clifford, L. Tarassenko, and L. A. Smith, “A dynamical model for generating synthetic electrocardiogram signals,” *IEEE Transactions on Biomedical Engineering*, vol. 50, no. 3, pp. 289–294, Mar. 2003.
- [59] W. Li and F. Yang, “Information fusion over network dynamics with unknown correlations: An overview,” *International Journal of Network Dynamics and Intelligence*, pp. 100 003–100 003, Jun. 2023.
- [60] A. Vaswani, N. Shazeer, N. Parmar, J. Uszkoreit, L. Jones, A. N. Gomez, Ł. Kaiser, and I. Polosukhin, “Attention is all you need,” *Advances in Neural Information Processing Systems*, vol. 30, 2017.
- [61] Y. Yao, L. Rosasco, and A. Caponnetto, “On early stopping in gradient descent learning,” *Constructive Approximation*, vol. 26, no. 2, pp. 289–315, Apr. 2007.
- [62] I. Loshchilov and F. Hutter, “SGDR: Stochastic gradient descent with warm restarts,” *arXiv preprint arXiv:1608.03983*, Aug. 2016.